

Order to Disorder in Quasiperiodic Composites

David Morison

*Department of Physics & Astronomy, University of Utah,
James Fletcher Building, 115 S 1400 E, Salt Lake City, UT 84112-0830*

N. Benjamin Murphy, Elena Cherkav, and Kenneth M. Golden

Department of Mathematics, University of Utah, 155 S 1400 E, Salt Lake City, UT 84112-0090

We introduce a novel class of two-phase composites that are structured by deterministic Moiré patterns, and display exotic behavior in their bulk electrical, magnetic, diffusive, thermal, and optical properties as system parameters are varied. The dependence of classical transport coefficients on mixture geometry is distilled into the spectral properties of an operator analogous to the Hamiltonian in quantum physics. As the system is tuned with a small change in the twist angle, there is a marked transition in the microstructure from periodic to quasiperiodic, and the transport properties switch from those of ordered to randomly disordered materials. Corresponding spectral properties such as eigenvalue spacing and field localization characteristics, viewed through the lens of random matrix theory, exhibit behavior analogous to an Anderson transition in wave phenomena, with band gaps and mobility edges — even though there are no wave scattering or interference effects at play here. Our findings establish a parallel between quantum transport in solids and classical transport in composite materials with periodic or quasiperiodic microstructure.

I. INTRODUCTION

In the late 1980s it was shown that in a composite patterned after a crystal, such as a dielectric material with a periodic lattice of voids, electromagnetic waves of certain frequencies and directions could be prohibited from propagating within the structure [1, 2]. This observation established a powerful analogy relating *photonic* band gaps to *electronic* band gaps in metals and other condensed matter. Thus solid state physics and Anderson localization was brought to optics [1–4], leading to the development of photonic crystals and theories of controlling the flow of light through structured media. The discovery of quasicrystals [5–7] demonstrated that geometries with predictable long range order but no periodicity could play an important role in physics and materials science. This led to the development of photonic quasicrystals [8–17], with the conceptual framework again provided by the analogy with quantum transport in solid state physics.

Motivated by these findings and the highly active field of twisted graphene bilayers [18], with Moiré patterns tuned by the twist angle to take periodic and aperiodic geometries, here we construct a class of deterministic, two-phase Moiré-structured composite materials in two dimensions. This construction enables us to study in several physical settings how classical transport behaves in the transition from periodicity to aperiodicity. Indeed, rather than a governing wave equation like Schrödinger’s equation for quantum transport or the classical wave equation for electromagnetic transport [17, 19–21], problems involving electrical conductivity σ , thermal conductivity κ , complex permittivity ϵ in the quasistatic limit, or diffusivity D can all be formulated in terms of the same divergence form second order elliptic equation (2) below, and do not involve any wave interference or scattering effects. Bulk behavior is analyzed in terms of the Bergman-Milton (or Stieltjes integral) representation, which holds for the effective parameters σ^* , κ^* , ϵ^* , D^* , etc. [22–25]. It involves a spectral measure μ of a self-adjoint operator G , which plays the role of the quantum physics Hamiltonian and depends only on the mixture geometry. In discrete settings, G is a real-symmetric matrix. The measure μ , local electric field \mathbf{E} , displacement $\mathbf{D} = \epsilon\mathbf{E}$ and current $\mathbf{J} = \sigma\mathbf{E}$ are all determined by the eigenvalues and eigenvectors of G . One of our main results is that through this spectral distillation and recent results on computing μ [26] and analyzing its behavior with random matrix theory [27], we establish a powerful analogy between various classical transport processes in periodic and quasiperiodic composites, and quantum transport with localization and band gaps in solid state physics, as was done for optics in photonic crystals and quasicrystals in the scattering regime. We emphasize, however, that our results apply broadly to transport phenomena in settings described by (2), with no restriction on the length scales in the systems involved, except for the condition imposed on the microstructural scale by the quasistatic assumption that must be satisfied in the context of complex permittivity.

We find that as the geometry is tuned from periodic to quasiperiodic, the eigenvalues, eigenmodes, profile of ϵ^* , and localization properties of \mathbf{E} undergo an order-to-disorder transition analogous to the Anderson transition. Our results are described in the (quasistatic) electromagnetic case, but we keep in mind their broad applicability. Spectral measures for periodic systems have sharp resonances that induce dramatic variability in band and absorption characteristics, and in profiles of ϵ^* . Regions of extended eigenstates are separated by “mobility edges” of localized states, and \mathbf{E} is localized for certain frequencies and extended for others. As the geometry is tuned to aperiodicity, the behavior of μ and ϵ^* resembles that of the 2D random percolation model at its threshold, with a regularly distributed

55 mixture of localized and extended eigenstates giving rise to tenuously connected current paths, pronounced spectral
 56 endpoint behavior, and Wigner-Dyson eigenvalue statistics with strong level repulsion [27].

57 Our investigation here of quasiperiodic media was motivated not only by the findings for random media in [27], but
 58 by much earlier studies which revealed sensitive, discontinuous dependence of bulk transport on the variations in local
 59 properties [28, 29]. For example, it was found in one dimension with local conductivity $\sigma(x) = 3 + \cos x + \cos kx$, which
 60 is periodic for k rational and quasiperiodic for k irrational, that the effective conductivity $\sigma^*(k)$ is discontinuous in k
 61 [28], with 2D examples in [29]. These studies, in turn, were motivated by the discovery of quasicrystals and findings
 62 on the spectrum of Hamiltonians with quasiperiodic potentials [30–32].

63 The spectral characteristics considered here govern the optical properties of nanostructured bimetallic films [33, 34]
 64 and depositions of nanosized metal particles on thin dielectric substrates [35–38], which change as a function of
 65 heterogeneous surface structure composition and geometry. This enables tunability of their optical responses for
 66 nano-plasmonic device applications [33–38]. The long wavelength quasistatic assumption holds in the visible range
 67 [39], and these systems are described macroscopically by the Stieltjes integral representations for ϵ^* or σ^* . Resonances
 68 in μ explain giant surface-enhanced Raman scattering observed in semicontinuous films [34, 40, 41], and induce strong
 69 fluctuations in \mathbf{E} and the dielectric profile of ϵ^* , associated with the excitation of collective electronic surface plasmon
 70 modes [39]. We numerically explore these phenomena in 2D impedance networks with quasiperiodic microgeometry
 71 and discuss our results using Anderson transition interpretations of random matrix theory.

72 II. METHODS

73 We begin by introducing a class of 2D two-component composites whose microgeometries are based on Moiré
 74 patterns, and are tunable to be periodic or aperiodic as follows. Consider the square bond lattice joining nearest
 75 neighbor points in \mathbb{Z}^2 , with standard basis vectors \mathbf{e}_1 and \mathbf{e}_2 , and the scaled rotation transformation T defined for
 76 $(x, y) \in \mathbb{R}^2$ by

$$T : (x, y) \mapsto (a, b), \quad T = r \begin{pmatrix} \cos \theta & -\sin \theta \\ \sin \theta & \cos \theta \end{pmatrix}. \quad (1)$$

77 The mixture geometry of the two phases is determined by the characteristic function χ_1 , taking the value $\chi_1 = 1$ in
 78 material phase 1 and zero otherwise, with $\chi_2 = 1 - \chi_1$. The system microgeometry is constructed from the periodic
 79 function $\psi(a, b) = \cos(2\pi a) \cos(2\pi b)$ and the condition $\chi_1(x, y) = 1$ for all $(x, y) \in \mathbb{R}^2$ such that $\psi(T(x, y)) \geq \psi_0$,
 80 and is zero otherwise. We focus on the value $\psi_0 = 0$, which generates in the underlying bond lattice a discretized

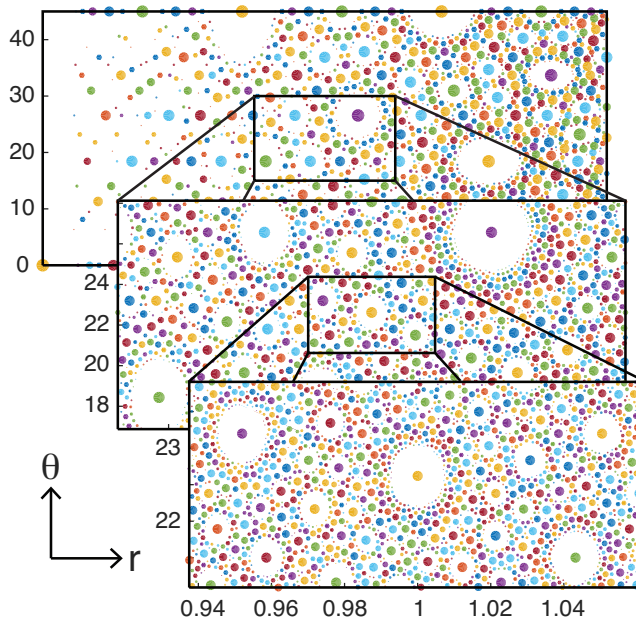


FIG. 1. **Fractal arrangement of periodic systems.** Sequential insets zooming into smaller regions of parameter space. Dots identify (r, θ) values corresponding to systems with periodic microgeometry, where short and large periods are identified by large and small dots, respectively, revealing self similar, fractal arrangements of periodic systems.

81 composite microstructure with a fraction $p \approx 1/2$ of type one bonds. We do so to compare features of deterministically
82 tuned quasiperiodic systems to those of the random percolation model near the percolation transition $p = p_c = 1/2$
83 [42, 43].

84 Primitive translation vectors for ψ are $\mathbf{t}_1 = (1/2, 1/2)$ and $\mathbf{t}_2 = (1/2, -1/2)$. When r and θ are chosen such that
85 $T : (m\mathbf{e}_1 + n\mathbf{e}_2) \mapsto (m'\mathbf{t}_1 + n'\mathbf{t}_2)$ for integer values of m, n, m' and n' , then χ_1 has a finite period of, at most,
86 $K = \sqrt{m^2 + n^2}$, and has infinite period otherwise. The arrangement of r and θ such that $K < \infty$ is fractal in nature,
87 as shown in Figure 1. The arrangement of (r, θ) values associated with finite periods is similar to fractal distributions
88 defined in terms of rational numbers on the real line, such as Thomae's function [29].

89 The effective behavior of macroscopic transport in two-phase composite materials is described by homogenized
90 coefficients including electrical and thermal conductivity, diffusivity, complex permittivity, and magnetic permeability.
91 These can all be defined in terms of the same elliptic partial differential equation [25, 43]. For complex permittivity in
92 the quasistatic regime, such as the metal-dielectric mixtures in visible light discussed above, the system is described
93 locally by

$$\nabla \cdot (\epsilon \nabla \phi) = 0, \quad (2)$$

94 with potential ϕ , electric field $\mathbf{E} = -\nabla \phi$, displacement $\mathbf{D} = \epsilon \mathbf{E}$, and local complex permittivity $\epsilon(x, y)$ taking
95 frequency dependent values $\epsilon_1(\omega)$ or $\epsilon_2(\omega)$, where $\langle \mathbf{E} \rangle = \mathbf{E}_0$ and $\langle \cdot \rangle$ denotes spatial average. The fields \mathbf{E} and \mathbf{D}
96 satisfy $\nabla \times \mathbf{E} = 0$ and $\nabla \cdot \mathbf{D} = 0$, with $\epsilon = \epsilon_1 \chi_1 + \epsilon_2 \chi_2$. See [24–26] for a “weak” formulation of this problem that
97 rigorously accounts for the discontinuous, and thus non-differentiable nature of the parameter $\epsilon(x, y)$ in equation (2).

98 The effective permittivity matrix ϵ^* can be defined by $\langle \mathbf{D} \rangle = \epsilon^* \langle \mathbf{E} \rangle$ with $\langle \mathbf{E} \rangle = \mathbf{E}_0$, where $\mathbf{E}_0 = E_0 \mathbf{e}_k$ for some
99 standard basis vector \mathbf{e}_k , $k = 1, \dots, d$, where d is dimension. Equivalently, it can be defined in terms of system energy
100 using $\langle \mathbf{D} \cdot \mathbf{E} \rangle = \epsilon_{kk}^* E_0^2$, where ϵ_{kk}^* is the k th diagonal coefficient of the matrix ϵ^* , which we denote by $\epsilon^* = \epsilon_{kk}^*$.
101 Thus, the effective parameter characterizes a homogeneous medium immersed in a uniform field \mathbf{E}_0 that behaves
102 macroscopically and energetically as does the inhomogeneous composite medium.

103 The key step in the analytic continuation method [22–26] is the Stieltjes integral representation for ϵ^* ,

$$F(s) = 1 - \frac{\epsilon^*}{\epsilon_2} = \int_0^1 \frac{d\mu(\lambda)}{s - \lambda}, \quad s = \frac{1}{1 - \epsilon_1/\epsilon_2}. \quad (3)$$

104 Here, $F(s) = \langle \chi_1 \mathbf{E} \cdot \mathbf{E}_0 \rangle / (sE_0^2)$ and $-F(s)$ plays the role of an effective electric susceptibility. Equation (3) follows
105 from applying the operator $-\nabla(-\Delta)^{-1}$ to equation (2) and writing it as $\Gamma \mathbf{D} = 0$, where $\Gamma = -\nabla(-\Delta)^{-1} \nabla \cdot$ is an
106 orthogonal projection onto curl-free fields and is based on convolution with the Green's function for the Laplacian
107 $\Delta = \nabla^2$ [24, 26]. Then using $\epsilon = \epsilon_1 \chi_1 + \epsilon_2 \chi_2 = \epsilon_2(1 - \chi_1/s)$ and $\Gamma \nabla \phi = \nabla \phi$ yields the resolvent representation

$$\chi_1 \mathbf{E} = s(sI - G)^{-1} \chi_1 \mathbf{E}_0, \quad G = \chi_1 \Gamma \chi_1, \quad (4)$$

108 involving the self-adjoint operator $G = \chi_1 \Gamma \chi_1$ [24, 26]. Applying the spectral theorem to $F(s) = \langle \chi_1 \mathbf{E} \cdot \mathbf{E}_0 \rangle / (sE_0^2)$
109 then yields [24, 26] equation (3), where μ is a spectral measure of the operator G .

110 A key feature of equations (3) and (4) is that the material parameters in s and the applied field strength E_0 are
111 separated from the geometric complexity of the system, which is encoded in the properties of the spectral measure μ
112 and its moments $\mu_n = \int_0^1 \lambda^n d\mu(\lambda)$. For example, $\mu_0 = \langle \chi_1 \rangle = p$, the volume fraction (or area fraction) of medium 1.
113 All of the effective coefficients of the composite material mentioned above are represented by Stieltjes integrals with
114 the same μ [44].

115 While the measure μ can include discrete and/or continuous components [25], it reduces to a weighted sum of
116 Dirac δ -functions $\delta(\lambda - \lambda_j)$ for media such as laminates, hierarchical coated cylinder and sphere assemblages, and
117 finite *RLC* impedance networks [22–26]. Here, we investigate effective transport properties of square two-component
118 impedance networks in 2D of size M with periodic and quasiperiodic microgeometry. In this setting, $G = \chi_1 \Gamma \chi_1$ is a
119 real-symmetric matrix of size $N = 2M^2$, χ_1 is a diagonal matrix with 1's and 0's along the diagonal corresponding to
120 impedance type, and $\Gamma = \nabla(\nabla^T \nabla)^{-1} \nabla^T$ is a projection matrix, where ∇ is a finite difference matrix representation
121 of the differential operator ∇ [26]. The measure μ is determined by the eigenvalues λ_j and eigenvectors \mathbf{v}_j of $N_1 \times N_1$
122 submatrices of Γ with rows and columns corresponding to the diagonal components $[\chi_1]_{jj} = 1$, with

$$d\mu(\lambda) = \sum_j m_j \delta(\lambda - \lambda_j) d\lambda, \quad m_j = (\mathbf{v}_j \cdot \chi_1 \hat{\mathbf{e}}_k)^2, \quad (5)$$

123 $j = 1, \dots, N_1$, $N_1 \approx pN$ (total number of ϵ_1 bonds), and $\hat{\mathbf{e}}_k$ is a standard basis vector in \mathbb{R}^{N_1} [26, 27]. In this case,
124 equations (3) and (4) become finite sums with

$$F(s) = 1 - \frac{\epsilon^*}{\epsilon_2} = \sum_j \frac{m_j}{s - \lambda_j}, \quad \chi_1 \mathbf{E} = sE_0 \sum_j \frac{(\mathbf{v}_j \cdot \chi_1 \hat{\mathbf{e}}_k)}{s - \lambda_j} \mathbf{v}_j, \quad (6)$$

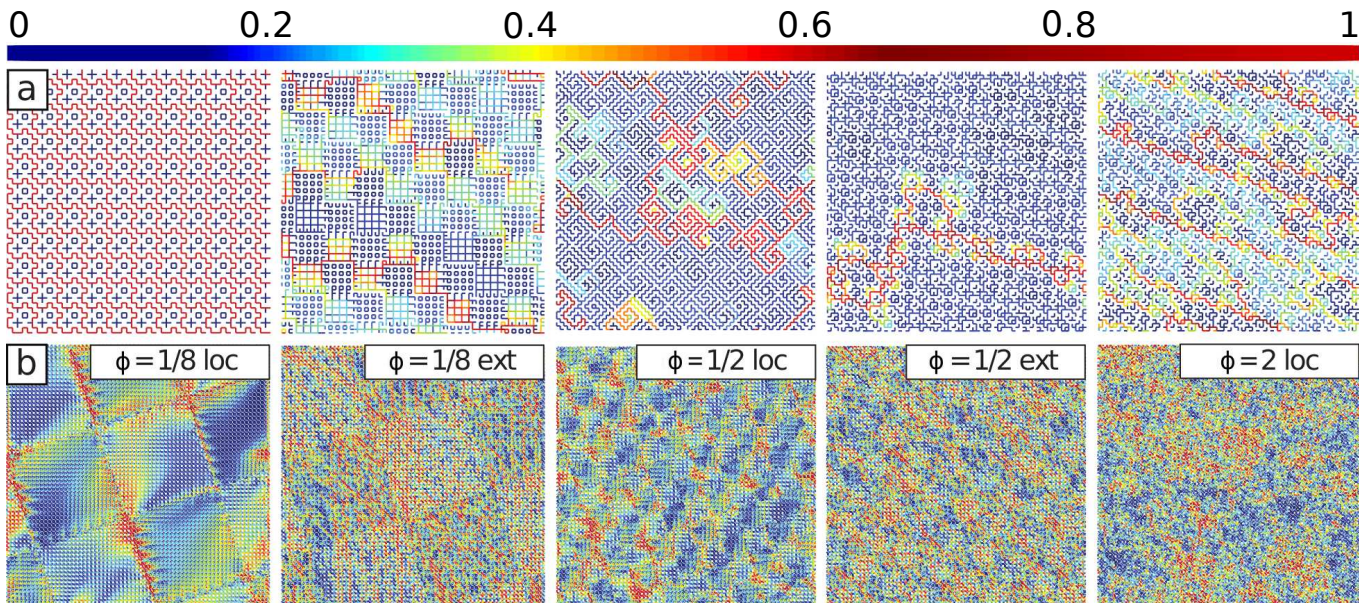


FIG. 2. **Quasiperiodic composite microgeometry and Anderson localization of fields.** Moiré interference patterns generated by the transformation (1) give rise to a large class of composite materials with periodic and quasiperiodic microgeometry. (a) Subsections of various examples (various r and θ) of such microgeometries are shown in (a) with square system sizes 53 for the far left and 73 for all others, small enough to resolve the small-scale detail yet illustrate the large geometric variety. Cool and warm colors correspond to near-zero and large values of $|\chi_1 \mathbf{E}|$ or $|\chi_1 \mathbf{D}|$, respectively, with the color bar at the top showing the saturated linear scale, normalized to the unit interval. (b) Anderson localization of fields in quasiperiodic media. Composite microgeometry parameterized by $r = \sqrt{10}/3$ and $\theta = \arctan(1/3) + \phi$ for $0^\circ \leq \phi \leq 2^\circ$ with system size 199. (In Figure 3 below, smaller subsets of these systems are displayed to show more small-scale detail.) For small values of ϕ , the fields exhibit a frequency dependent transition from localized (loc) to extended (ext). Identical values of ϕ correspond to identical microgeometries, and the differences in the values of $|\chi_1 \mathbf{E}|$ are solely due to frequency dependent material properties for different values of ω . As $\phi \rightarrow 2$, the local fields become similar for all frequencies away from $\omega = 0$, qualitatively resembling the rightmost panel in (b) (as well as that of the percolation model near the percolation threshold $p = p_c$ [27]). In discussions of Figures 3 and 5 below, we provide a quantitative description of this localization phenomenon.

125 given explicitly in terms of the λ_j and eigenvectors \mathbf{v}_j of G [26].

126 In the next section, we compute the spectral measure μ , hence the local fields and the effective complex permittivity
 127 ϵ^* for the Moiré-structured class of composite materials described by equation (1) above. We interpret the frequency
 128 dependent behavior of physical quantities such as the phase and amplitude of ϵ^* , and localization and intensity of \mathbf{E}
 129 and \mathbf{D} , in terms of spectral properties of μ and Anderson transition interpretations of random matrix theory.

130 III. RESULTS

131 The Moiré system introduced above is parameterized by $r > 0$ and $0 \leq \theta < 2\pi$, which generates a diverse
 132 assortment of periodic (“finite period”) and quasiperiodic (“infinite period”) microgeometries. To numerically calculate
 133 mathematical and physical quantities, we consider finite subsets of these systems as *RLC* impedance networks.
 134 Different types of microgeometries in this class are displayed in Figure 2a with small enough system sizes to resolve
 135 the small-scale geometry while still illustrating the large variety in structure, hinting at the geometric richness of our
 136 Moiré composites. The bond color indicates the *modulus* value of \mathbf{E} in phase 1, i.e., $|\chi_1 \mathbf{E}|$, calculated via (6). Since
 137 $\chi_1 \mathbf{D} = \epsilon_1 \chi_1 \mathbf{E}$ these colors also specify displacement values with a change in scale by $|\epsilon_1|$. We therefore normalize the
 138 computed fields to take values in the unit interval.

139 It was shown in [26] that expressions known in closed form for the 2D percolation model in the infinite volume
 140 limit are well approximated by ensemble averages of systems of size ≈ 70 and by single systems of size ≈ 200 . The
 141 Moiré-structured composites studied here can have coherent structures on large length scales. However, we found for
 142 a system size of 199 that fluctuations present for smaller systems have essentially stabilized, with numerical results
 143 visually identical for larger system sizes, e.g., ≈ 250 . A systematic study of system size dependence of quantities and
 144 finite size effects is interesting and useful but beyond the scope of the current manuscript.

145 In this section, we investigate a small swath of the large parameter space, for $r = \sqrt{10}/3$ and $\theta = \arctan(1/3) + \phi$

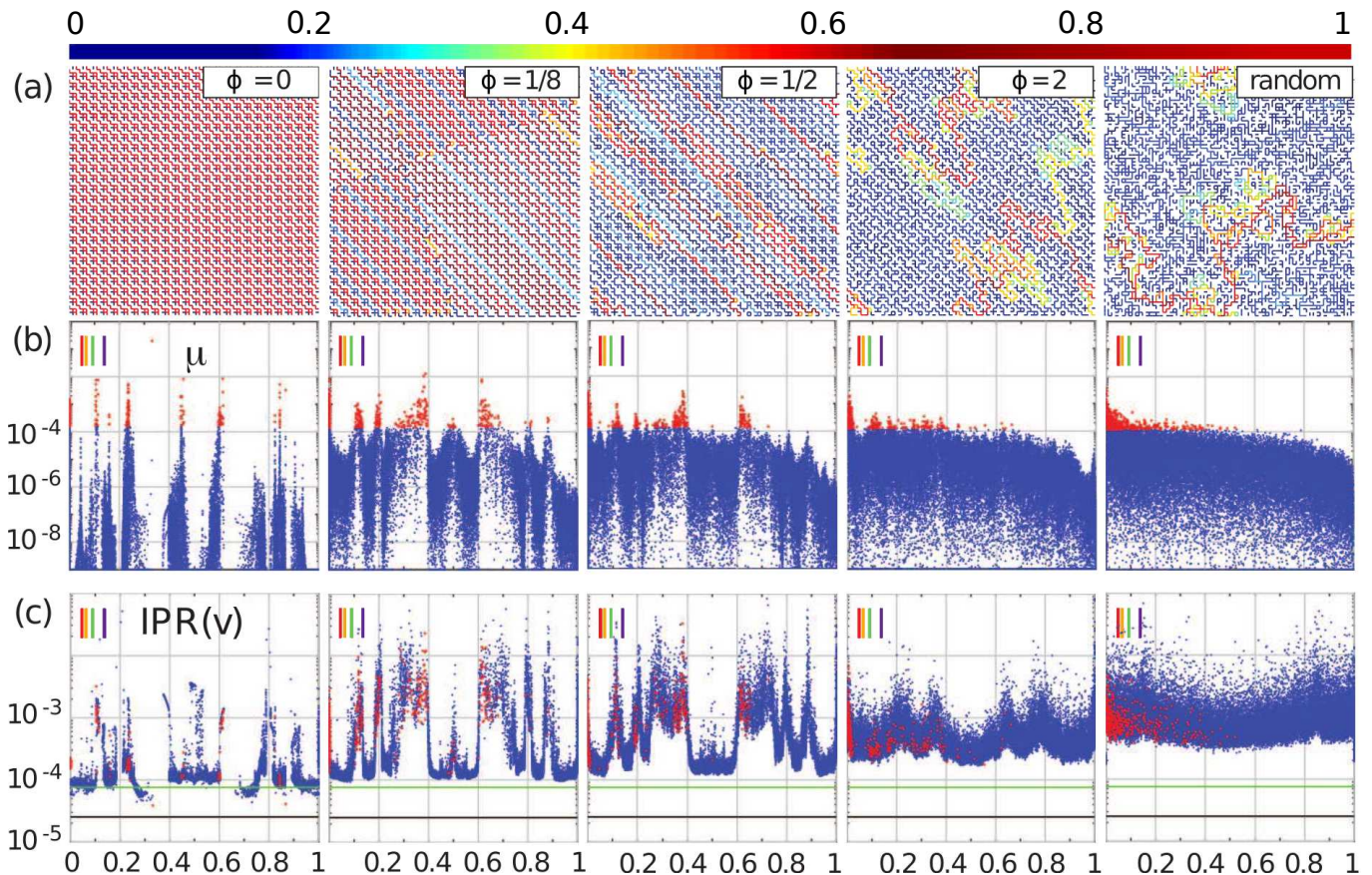


FIG. 3. **Frequency profile of the spectral measure and eigenvector localization.** Composite microgeometry and fields, spectral measure μ , and eigenvector IPR plotted for various values of the Moiré twist angle θ , for $0^\circ \leq \phi \leq 2^\circ$, $r = \sqrt{10}/3$, and square system of size 73 in (a) to show detail and of size 199 in (b) and (c). The color bars in the upper left of the panels are for reference and indicate $Re s(\omega)$ for the optical frequency range for impedances corresponding to the Drude model for a gold/vacuum composite. (a) Composite microgeometry and field intensity. Cool and warm colors correspond to near-zero and large values of $|\chi_1 \mathbf{E}|$ or $|\chi_1 \mathbf{D}|$, respectively, with color bar at the top showing the saturated linear scale. (b) Masses m_j of μ plotted *vs.* eigenvalues $0 \leq \lambda_j \leq 1$ of the matrix G . Red dots indicate the largest masses, used as indicators in (c) below. (c) IPR values for the eigenvectors \mathbf{v}_j of G , $IPR(\mathbf{v})$, plotted *vs.* λ_j . Green and black horizontal lines indicate IPR values for GOE and completely extended vectors, $3/N_1$ and $1/N_1$, respectively. These quantities for the random percolation model at the percolation transition, $p = p_c = 1/2$, are shown in the rightmost panels for comparison.

146 for $0^\circ \leq \phi \leq 2^\circ$, starting from a short period system. Figures 2b and 3a display examples of this region of parameter
 147 space and show that such a small change in the Moiré twist angle θ gives rise to a dramatic transition in composite
 148 microgeometry — from a short period system with orderly field (or current) paths to quasiperiodic systems with
 149 disorderly, meandering paths similar to those exhibited by the random percolation model near $p = p_c$.

150 When the fields are plotted *vs.* $s(\omega)$, $0 \leq Re s(\omega) \leq 1$ with $Im s(\omega) \ll 1$ a frequency dependent localization/
 151 delocalization transition of fields is revealed for small values of $\phi \in [0, 2]$, as shown in Figure 2b for $\phi = 1/8$ and
 152 $1/2$. In contrast, the fields for angles closer to $\phi = 2$ are more disordered and resemble those in the random percolation
 153 model, and are qualitatively similar to the rightmost panel in Figure 2b for all $0 < Re s \leq 1$. We investigate these
 154 and other phenomena through mathematical and physical quantities such as the spectral measure μ , correlations of
 155 its eigenvalues, localization of its eigenvectors, phase and magnitude of ϵ^* , localization and intensity of \mathbf{E} , etc.

156 A large variety of physical phenomena exhibited by inhomogeneous materials can be described by two component
 157 RLC impedance networks [40]. Each of the two components is created by combining a resistor R , inductor L , and
 158 capacitor C in a way that achieves an impedance characteristic of the material being modeled. For example, a Drude-
 159 metal/dielectric composite is modeled by R and L in series, in parallel with C for one component, and C for the other
 160 [39], yielding a plasma frequency $\omega_p^2 = 1/LC$ and relaxation time $\tau = L/R$. As Kirchhoff's network laws are discrete
 161 versions of the curl-free and divergence-free conditions on the fields in equation (1), these RLC impedance networks
 162 really do resemble the continuum composites they are intended to model [39].

163 Indeed, the AC response and polarization effects observed in a variety of conductor-dielectric mixtures at low

164 frequencies are modeled by an R - C network, while metal-dielectric composites exhibiting collective electronic modes
 165 at higher, optical frequencies such as (surface) plasmon resonances are modeled by an RL - C network [40, 41]. The
 166 dependence of $s(\omega)$ on frequency ω is model specific. For the R - C and RL - C models, $0 \leq Re s < 1$ for $0 \leq \omega < \infty$
 167 and $\delta \leq Im s < 0$, where $|\delta|$ can be chosen as small as desired, with $Re s \rightarrow 1$ and $Im s \rightarrow 0$ as ω increases [40, 41].
 168 In order to give a model independent description of the phenomena investigated here, we plot s -dependent quantities
 169 using $0 \leq Re s \leq 1$ and $Im s = 0.001$ fixed. For the sake of discussion, we describe our results in terms of the optical
 170 regime for the Drude model for gold/vacuum composites, which roughly corresponds to the interval $Re s \lesssim 0.2$. The
 171 optical regime for other material combinations corresponds to values of $Re s$ throughout the unit interval [45].

172 As the frequency changes and $s(\omega)$ sweeps across the complex plane, with $s(0) = 0$, the spectral measure μ ,
 173 distribution of its eigenvalues, and localization properties of its eigenvectors, shown in Figure 3, govern the frequency
 174 dependence of the phase and magnitude of ϵ^* and the intensity and localization of \mathbf{E} and \mathbf{D} , shown in Figure 5,
 175 according to the formulas in equation (6). Keeping these formulas with $Im s(\omega) \ll 1$ in mind, we call *resonant*
 176 *frequencies* the values of ω where $Re s(\omega) \approx \lambda_j$ and the masses m_j of μ are largest (shown in red in Figure 3) and/or
 177 there's a large density of eigenvalues λ_j with moderate to large values of m_j .

178 For the short period system with $\phi = 0$ shown in Figure 3a, the spectral measure μ in Figure 3b is comprised of
 179 sharply peaked resonances. As ϕ increases and the composite microgeometry becomes quasiperiodic, the resonant
 180 frequencies away from $\omega = 0$ ($\lambda = 0$) spread out, change frequency locations, and diminish in strength. As $\phi \rightarrow 2$,
 181 the resonances in μ continue to spread out until all but the Drude resonance at $\omega = 0$ diminish, and μ and ϵ^* begin
 182 to resemble those of the random percolation model for $p = p_c$, shown in the rightmost panels of Figure 3.

183 Resonances in μ have a physical interpretation in terms of relaxation times in the transient response in the R - C
 184 model, or in terms of dielectric resonances in the RL - C model [40, 41]. The dielectric resonances observed for the RL - C
 185 model with percolative geometry have been argued to provide a natural explanation for the anomalous fluctuations
 186 of the local electric field \mathbf{E} , which are responsible for giant surface-enhanced Raman scattering observed, for example,
 187 in semicontinuous metal films [41]. Below, we show that the resonances in μ shown in Figure 3 give rise to dramatic
 188 fluctuations in the amplitude and phase of ϵ^* and the intensity of the fields \mathbf{E} and \mathbf{D} .

189 The inverse participation ratio (IPR) characterizes vector *localization* phenomenon. For an N_1 -dimensional unit
 190 vector \mathbf{u} it is given by $IPR(\mathbf{u}) = \sum_i u_i^4$, where u_i is the i th component of the vector \mathbf{u} , $i = 1, \dots, N_1$, and satisfies
 191 $IPR(\mathbf{u}) = 1$ for a completely localized vector with only one non-zero component and $IPR(\mathbf{u}) = 1/N_1$ for a completely
 192 extended vector with all components equal in value [27]. For matrices in the Gaussian orthogonal ensemble (GOE),
 193 the eigenvectors are quite extended with a mean asymptotic IPR value of $IPR_{GOE} = 3/N_1$ [27].

194 Figure 3c displays $IPR(\mathbf{v}_j)$ for the eigenvectors \mathbf{v}_j , $j = 1, \dots, N_1$, of G for various values of ϕ , as a function of
 195 the eigenvalues λ_j . The red dots in Figures 3b and 3c for $\phi = 0$ and $1/8$ show that resonant frequencies correspond
 196 either to very extended eigenvectors or “mobility edges” where the values $IPR(\mathbf{v}_j)$ have large variability for small
 197 changes in λ_j . As ϕ increases and the microgeometry becomes quasiperiodic, the mobility edges diminish as the values
 198 $IPR(\mathbf{v}_j)$ become more regularly distributed and qualitatively similar for all $0 < Re s(\omega) \leq 1$ away from the Drude
 199 peak at $\omega = 0$, as shown in the two rightmost panels of Figure 3b. As $\phi \rightarrow 2$, the $IPR(\mathbf{v}_j)$ resemble those of the
 200 random percolation model at its threshold $p = p_c = 1/2$, as shown in the rightmost panel of Figure 3c.

201 The frequencies corresponding to resonances of μ and field delocalization are tunable through the quasiperiodic
 202 microgeometry via the scale parameter r and Moiré twist angle θ in (1), which is critical to potential engineering
 203 applications — given a desired frequency dependence for the profile of ϵ^* and field localization, values of r and θ can be
 204 selected accordingly. This is illustrated in Figure 4 which displays the θ -dependence of the eigenvalue density $\rho(\lambda, \theta)$
 205 in (a), the spectral function $\mu(\lambda, \theta)$ in (b), the magnitude and phase of the relative effective permittivity ϵ^*/ϵ_2 in (c)
 206 and (d) and the IPR in (e), with $r = \sqrt{5}/2$ fixed. Short period systems are indicated by dark horizontal streaks due
 207 to associated isolated resonances in μ , with localized regions of yellow. Figure 4a shows that some of these resonances
 208 in $\mu(\lambda, \theta)$ are due to resonances in $\rho(\lambda, \theta)$. However, in Figure 4b, the significance of the measure mass becomes
 209 apparent, which can diminish eigenvalue resonances or even create resonances in $\mu(\lambda, \theta)$ in regions of low eigenvalue
 210 density — also illustrated in the leftmost panel of Figure 3b by the individual eigenvalue $\lambda_j \approx 0.32$ with relatively
 211 large spectral mass $m_j \gtrsim 0.1$. The influence of μ on ϵ^*/ϵ_2 is striking with resonances and features in $|\epsilon^*/\epsilon_2|$ following
 212 those in μ , and with an antisymmetry in phase(ϵ^*/ϵ_2) about $Re s \approx 0.5$. The IPR values displayed in Figure 4e again
 213 illustrate that resonances in μ are associated either with extremely extended eigenvectors or mobility edges, with
 214 large variability in IPR values for a small change in λ . The symmetry $\rho(\lambda) = \rho(1 - \lambda)$ well known for the percolation
 215 model [26, 41] is evident in Figure 4a for quasiperiodic geometry, and also has symmetry for θ between $\pi/8$ and $3\pi/16$
 216 reminiscent of, but distinctly different from, the Hofstadter-like spectral butterflies observed in the spectra for twisted
 217 bilayers and Bloch electrons in magnetic fields [21]. The distinct anomaly in the other figure panels associated with
 218 this “butterfly” is due to a region of parameter space associated with very short system period. A careful comparison
 219 of the visual features between the eigenvalue density and eigenvector IPR strongly suggests significant correlations
 220 between the eigenvalues and eigenvectors.

221 The eigenvector expansion of $\chi_1 \mathbf{E}$ in equation (6) provides a clear connection between resonant frequencies and

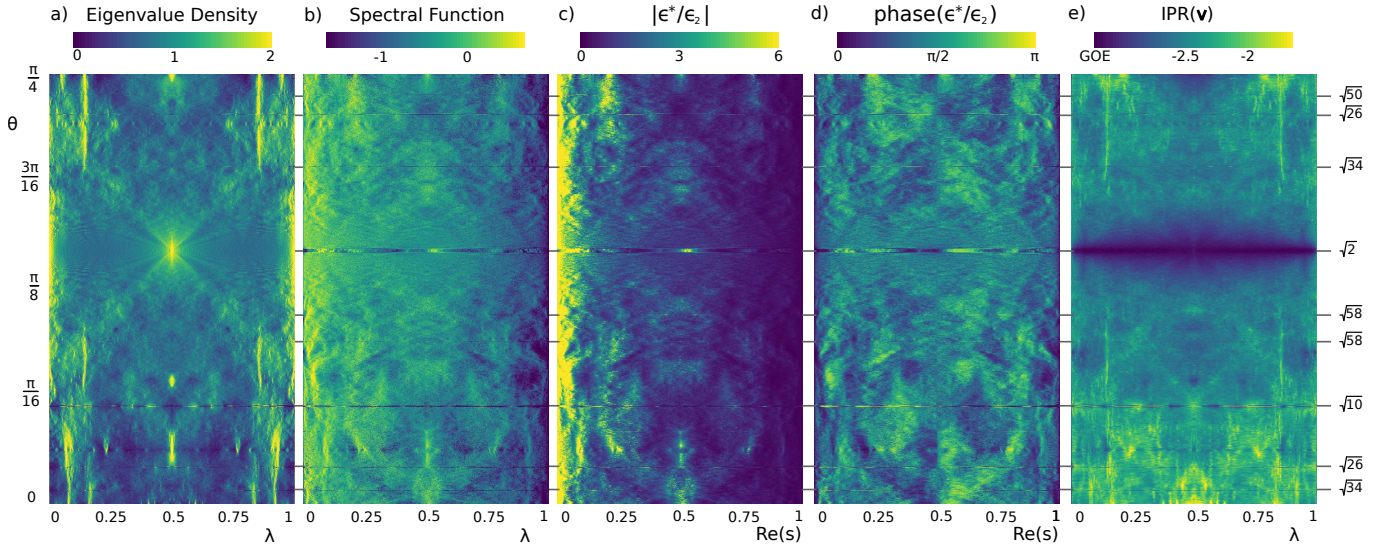


FIG. 4. **Twist angle dependence of the eigenvalue density, spectral function, effective permittivity, and IPR .** (a) Eigenvalue density $\rho(\lambda, \theta)$ (a histogram representation of the density of states $\sum_j \delta(\lambda - \lambda_j)/N_1$), (b) the spectral function $\mu(\lambda, \theta)$ (a kernel estimate representation of the spectral measure), (c) magnitude and (d) phase of relative effective complex permittivity ϵ^*/ϵ_2 , and (e) a histogram-like representation of the IPR (median IPR of eigenstates associated with each bin — to distinguish mobility edges), all plotted *vs.* the Moiré twist angle θ for $r = \sqrt{5}/2$. We plot these quantities for one full period $0 \leq \theta \leq \pi/4$. (a), (b), and (e) are plotted *vs.* $0 \leq \lambda \leq 1$, while (c) and (d) are plotted versus $0 \leq Re\ s \leq 1$ for $Im\ s = 0.001$. Low and high density for ρ and μ are indicated by dark blue and yellow, respectively, as shown by the color bars (with linear scale in (a), (c), and (e) and \log_{10} scale in (b) and (e), slightly saturated at the ends to reveal more detail). Short period systems appear as horizontal streaks; for ρ and μ sharp isolated resonances are identified by localized yellow resonant peaks surrounded by dark blue troughs with values orders of magnitude smaller. The influence of μ on ϵ^*/ϵ_2 is clear, with striking similarities. For the IPR in (e) extended and localized vectors are identified by dark blue (with GOE value labeled) and yellow, with mobility edges indicated by sudden changes from one extreme to the other. Some of the θ values associated with these short period systems are identified by black tick marks on the right, labeled by the bound $K = \sqrt{m^2 + n^2}$ on the system period, discussed in Section II.

222 large field intensity when $Im\ s(\omega) \ll 1$. However, our analysis of Figure 3 also indicates these resonant frequencies
 223 correspond to fields that are either extended throughout the medium, as in the leftmost panel of Figure 3a, or to a
 224 mixture of localized and extended states giving rise to more spatially varied field characteristics in both the intensity
 225 and localization, as in the leftmost panel of Figure 2b, with sensitive dependence on frequency.

226 We now make this correspondence more precise in an analysis of the magnitude and phase of ϵ^* and the localization
 227 of \mathbf{E} and \mathbf{D} . They are displayed in Figure 5 for various values of the Moiré twist angle θ , for $0^\circ \leq \phi \leq 2^\circ$, as
 228 a function of $Re\ s(\omega)$. The Drude peak at $\omega = 0$ ($s(0) = 0$) present for all values of ϕ indicates the composite is
 229 conducting for $\omega = 0$ [39]. For $\phi = 0$, at the resonant frequencies both μ and $|\epsilon^*|$ are sharply peaked and ϵ^* diverges
 230 as $Im\ s \rightarrow 0$. These frequencies correspond to the so-called surface plasmon resonance, which characteristically shows
 231 up as a strong absorption line in experiments [39]. At these resonant frequencies ϵ^* also undergoes a dramatic switch
 232 in phase which gives rise to an “optical transition,” where the material response changes from inductive (metallic)
 233 to capacitive (dielectric) — a phenomenon observed in optical cermet [40]. These phase switches also occur at the
 234 troughs of $|\epsilon^*|$, where $|\epsilon^*|$ and the mass of μ are small. At these *band gap* frequencies the material behaves effectively
 235 like an electrical insulator. As ϕ increases, the transition frequencies still correspond to the peaks and troughs in $|\epsilon^*|$,
 236 though the frequency dependence of these features becomes more irregular.

237 The IPR for $|\chi_1 \mathbf{E}|$ (normalized to unit length) provides a measurement of localization for the electric field it-
 238 self — equivalently for the normalized displacement field $\chi_1 \mathbf{D} = \epsilon_1 \chi_1 \mathbf{E}$. Figures 3c and 5b show there is a close
 239 relationship between the eigenvector IPR , $IPR(\mathbf{v})$, plotted *vs.* λ_j and the electric field IPR , $IPR(\mathbf{E})$, plotted *vs.*
 240 $Re\ s(\omega)$, as anticipated above. Specifically, there are frequency regions where the eigenmodes and the electric field
 241 are simultaneously localized or extended. Moreover, for $\phi = 0, 1/8$, and $1/2$ there are several clear mobility edges
 242 in $IPR(\mathbf{E})$, following those in $IPR(\mathbf{v})$, showing high variability in field localization for small changes in $s(\omega)$, which
 243 also correspond to resonant frequencies and high variability in field intensity.

244 In Figure 2b the localized (loc) and extended (ext) fields for $\phi = 1/8, 1/2$, and 2 were computed for values of
 245 $Re\ s(\omega)$ with optical frequencies ω — indicated by red dots in Figure 5. Comparing these two figures for the panels
 246 with values $\phi = 1/8$ and $1/2$ further demonstrates the frequency dependent localization/delocalization transition in

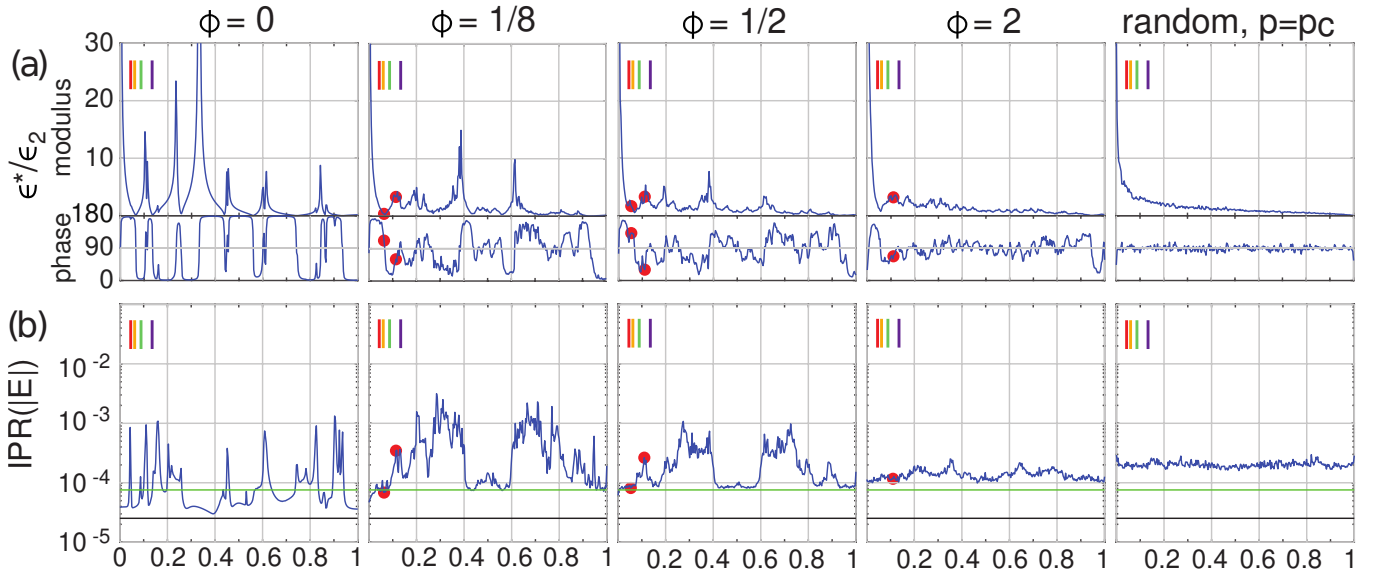


FIG. 5. **Frequency dependence of dielectric profile and field localization.** Relative effective complex permittivity ϵ^*/ϵ_2 and IPR of the modulus of the electric field, $|\chi_1 \mathbf{E}|$, normalized to unity, $IPR(\mathbf{E})$, plotted versus $0 \leq Re s \leq 1$ for $Im s = 0.001$ and various values of the Moiré twist angle θ and $r = \sqrt{10}/3$, for $0^\circ \leq \phi \leq 2^\circ$. The color bars in the upper left of the panels are for reference and indicate $Re s(\omega)$ for the optical frequency range for impedances corresponding to the Drude model for a gold/vacuum composite. (a) Amplitude and phase of ϵ^*/ϵ_2 . (b) $IPR(\mathbf{E})$ or equivalently $IPR(\mathbf{D})$. These quantities for the random percolation model at the percolation transition, $p = p_c = 1/2$, are shown in the rightmost panels for comparison. The red dots in (a) and (b) identify values of $Re s$ used in Figure 2b: for $\phi = 1/8$, $Re s = 0.063, 0.115$, for $\phi = 1/2$, $Re s = 0.055, 0.111$, and for $\phi = 2$, $Re s = 0.111$.

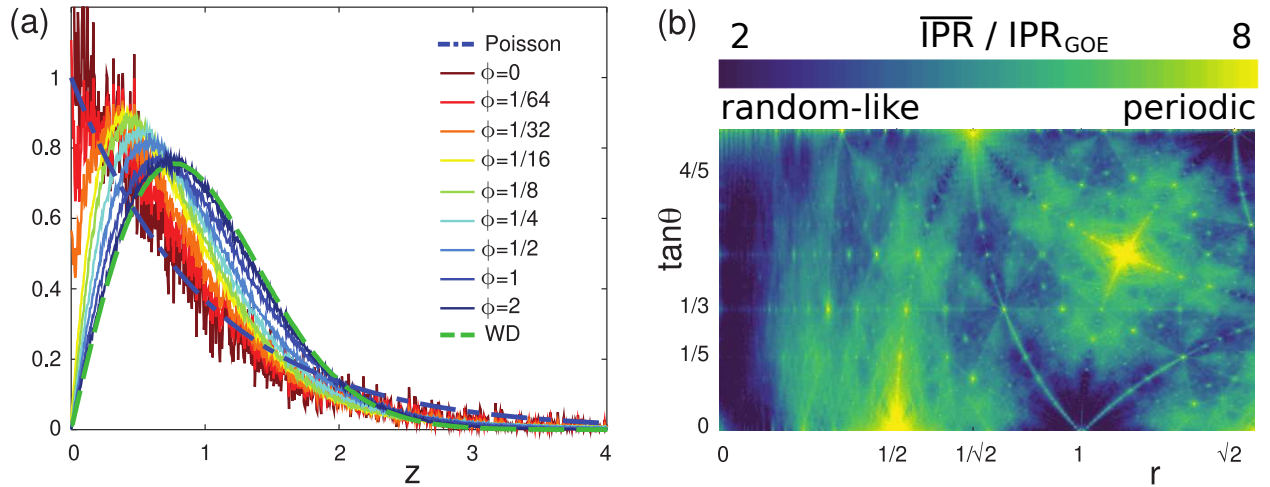


FIG. 6. **Eigenvalue spacings and eigenvector localization.** (a) The eigenvalue spacing distribution (ESD) $P(z)$ for various values of (Moiré) twist angle θ , for $0^\circ \leq \phi \leq 2^\circ$. The short period system for $\phi = 0$ and those with small twist angles $0 \leq \phi \leq 1/32$ are characterized by spectral measures μ with very sharp resonances leading to $P(0) \gtrsim 0.4$. However, for $\phi \geq 1/16$ the system begins to transition towards obeying WD statistics with level repulsion, so that $P(0) = 0$. Level repulsion increases with increasing ϕ as the ESD approaches the WD ESD, characterized by strong correlations and strong eigenvalue repulsion. (b) The ratio of average eigenvector \overline{IPR} with $IPR_{GOE} = 3/N_1$ is plotted vs. $(r, \tan \theta)$. Yellow hues correspond to short period systems similar to the leftmost panel in Figure 2, characterized by highly extended eigenmodes (hence extended electric and displacement fields) and “mobility edges” with large localization variability. Dark green to blue hues correspond to quasiperiodic systems similar to the one shown in Figure 2 for $\phi = 2$ with material properties that resemble that of random systems with regularly distributed IPR values and tenuously connected electric and displacement field paths. This panel indicates periodic systems have a repeating pattern that turns out to be fractal in nature, as indicated in Figure 1. Moreover, quite small changes in the Moiré parameters $(r, \tan \theta)$ result in transitions from ordered periodic systems to disordered quasiperiodic, random-like systems.

the displacement field *for the same microstructure*. Moreover, the panels for localized (loc) fields in Figure 2b also correspond to resonant peaks in μ in Figure 3b, which accounts for the high variability in the field intensity in Figure 2b and the amplitude of ϵ^* in Figure 5a. Furthermore, Figure 5 for $\phi = 1/8$ and $1/2$, shows that toward the infrared end of the spectrum the displacement field is extended and the response of ϵ^* is inductive (metallic), while toward the ultraviolet end of the spectrum the displacement field is more localized and the response of ϵ^* is capacitive (dielectric). There are also band gap frequencies in the optical range.

As ϕ surpasses $1/8$, band gap frequencies are absent. The larger checkerboard scale for $|\chi_1 \mathbf{E}|$ shown in Figure 2b decreases in size and all the material characteristics described above begin to qualitatively resemble those of the random percolation model for $p = p_c$ as $\phi \rightarrow 2$. The more regularly distributed eigenvector localization gives rise to spatially varied, meandering, tenuously connected field paths as shown in the corresponding panels of Figure 3a.

These observations indicate a high degree of *tunability* in the frequency dependence of the phase and magnitude of ϵ^* and the localization and intensity of \mathbf{E} and \mathbf{D} . The resonant and band gap frequencies present for small ϕ are tunable through the microstructure itself via the scale r and Moiré twist angle θ in (1). We predict that these material characteristics can be reproduced experimentally and tuned by fabrication methods used for etched metallic substrates. (In [46], a small change in Moiré twist angle for bilayer graphene induces a change in conductivity similar to what we observe here for ϵ^* .) Since the transformation in equation (1) is deterministic, one can also obtain material characteristics similar to those of random systems in a predictable, reproducible manner. This tunability makes our Moiré-type composite class an ideal test bed for potential engineering applications.

Statistical quantities for the eigenvalues λ_j of μ provide insights into why the high density resonances of μ , present for the short period system with $\phi = 0$, spread out as ϕ increases and the system becomes quasiperiodic. The nearest neighbor eigenvalue spacing distribution (ESD) $P(z)$ was initially introduced in random matrix theory to describe fluctuations of characteristic quantities for random systems, but has since accurately described quantities for non-random systems with sufficient complexity [47]. The ESD probes short range correlations of eigenvalues [47]. For highly correlated Wigner-Dyson (WD) spectra exhibited by, for example, the Gaussian orthogonal ensemble (GOE) of real-symmetric random matrices, the ESD is accurately approximated by $P(z) \approx (\pi z/2) \exp(-\pi z^2/2)$, Wigner's surmise, which illustrates *eigenvalue repulsion*, vanishing linearly as spacings $z \rightarrow 0$ [47, 48]. In contrast, the ESD for uncorrelated Poisson spectra, $P(z) = \exp(-z)$, allows for significant level degeneracy [47].

Figure 6a displays the ESD for the eigenvalues λ_j of G for several values of $0^\circ \leq \phi \leq 2^\circ$. The blue dash-dot curve is the ESD for Poisson spectra, while the green dashed curve is the ESD for the GOE. For $\phi = 0, 1/64$, and $1/32$, the sharply peaked resonances in μ with high eigenvalue density give rise to a significant probability of zero spacings, with $P(0) \gtrsim 0.4$. However, as ϕ increases and the composite microgeometry becomes quasiperiodic, the behavior of the ESDs starts to be characterized by weakly correlated Poisson-like statistics [48], also observed for eigenvalues of G for the low volume fraction percolation model [27]. They increase linearly from zero but the initial slope of $P(z)$ is steeper than in the WD case, implying less level repulsion. As $\phi \rightarrow 2$, the slope of $P(z)$ decreases, indicating an increase in level repulsion, causing the eigenvalues of μ to spread out as the ESD transitions toward obeying that of the GOE, characterized by highly correlated eigenvalues with strong level repulsion.

We conclude this section with a discussion of Figure 6b, which displays the average eigenvector *IPR* with yellow hues corresponding to short period systems with highly extended eigenmodes — hence displacement fields — and mobility edges, and dark green to blue hues corresponding to quasiperiodic, random-like systems with more regularly distributed eigenmodes and meandering, tenuously connected field paths. Our results here are only a snapshot, which nevertheless reveals the great diversity of this class of composite materials with myriad microgeometric variations, each with a potentially distinct frequency dependence in both the phase and magnitude of ϵ^* and the localization and intensity of \mathbf{E} and \mathbf{D} . Figure 1 shows that the arrangement of finite period systems is fractal in nature. It is clear from Figures 1 and 6b that we have merely scratched the surface in describing this fascinating class of composite materials with tuneable capabilities in both frequency and geometry, potentially enabling materials to be fabricated that achieve desired field characteristics and dielectric responses suitable for a broad range of engineering applications.

IV. CONCLUSION

A novel class of Moiré-structured 2D composite materials is introduced. Bulk transport is explored using a Stieltjes integral representation for the effective transport coefficients, and the complex permittivity ϵ^* in particular. The representation involves a spectral measure μ of a real-symmetric matrix G , and a summation formula for the displacement field \mathbf{D} , involving the eigenvalues λ_i and eigenvectors \mathbf{v}_i of G . The localization properties of \mathbf{D} and the dielectric profile for ϵ^* are analyzed as the Moiré twist angle θ varies 2 degrees. This small change in θ gives rise to a sharp transition in the microgeometry of the composite material, from periodic to quasiperiodic as the period increases *ad infinitum*. Short period systems are characterized by sharp resonances in μ which give rise to optical frequencies ω where ϵ^* is sharply peaked (so-called surface plasmon resonance frequencies) and ϵ^* undergoes an “optical transition”

from inductive (metallic) to capacitive (dielectric). Band gap optical frequencies are also observed. Moreover, \mathbf{D} is highly extended for certain ranges of frequency, separated by small “mobility edge” frequency regions of large localization variability, that follow the resonant peaks of μ with high intensity regions of \mathbf{D} . These characteristics make the dielectric profile and field response highly tunable, a desired feature in engineering applications. As the system is tuned to quasiperiodicity, an increase in eigenvalue repulsion, as measured by the eigenvalue spacing distribution (ESD), causes the sharp resonances of μ to spread out, while the localization characteristics of \mathbf{D} and the dielectric profile of ϵ^* begin to qualitatively resemble those of the percolation model near its transition point. It is suggested that these material characteristics could be reproduced experimentally and tuned by fabrication methods used for etched metallic substrates.

Acknowledgments. We gratefully acknowledge support from the Division of Mathematical Sciences at the U.S. National Science Foundation through Grant DMS-1715680 and the Office of Naval Research Applied and Computational Analysis Program through Grants N00014-18-1-2552 and N00014-21-1-2909. We thank Valy Vardeny and Sarah Li for helpful conversations. We also thank one of the reviewers for suggesting the creation of Figure 4. Finally, we would like to thank Joel Lebowitz and Shelly Goldstein for originally asking the question about the behavior of classical transport in quasiperiodic media almost four decades ago, which helped lead to the current investigation.

V. CODE AVAILABILITY

Mathematical and numerical methods used to compute the spectral measures and associated spectral statistics displayed in this manuscript are detailed in [26]. Associated code will be made available upon reasonable request.

VI. DATA AVAILABILITY

Numerical data used to generate figures in this manuscript will be made available upon reasonable request.

-
- [1] Yablonovitch, E. Inhibited spontaneous emission in solid-state physics and electronics. *Phys. Rev. Lett.* **58**, 2059–2062 (1987).
 - [2] Yablonovitch, E. & Gmitter, T. J. Photonic band structure: the face-centered-cubic case. *Phys. Rev. Lett.* **63**, 1950–1953 (1989).
 - [3] John, S. Strong localization of photons in certain disordered dielectric superlattices. *Phys. Rev. Lett.* **58**, 2486–2489 (1987).
 - [4] Ioannopoulos, J. D., Johnson, S. G., Winn, J. N. & Meade, R. D. *Photonic Crystals: Molding the Flow of Light, Second Edition* (Princeton University Press, 2008).
 - [5] Shechtman, D., Blech, I., Gratias, D. & Cahn, J. W. Metallic phase with long-range orientational order and no translational symmetry. *Phys. Rev. Lett.* **53**, 1951–1953 (1984).
 - [6] Levine, D. & Steinhardt, P. J. Quasicrystals: A new class of ordered structures. *Phys. Rev. Lett.* **53**, 2477–2480 (1984).
 - [7] Dubois, J.-M. Properties and applications of quasicrystals and complex metallic alloys. *Chem. Soc. Rev.* **41**, 6760–6777 (2012).
 - [8] Vardeny, Z. V., Nahata, A. & Agrawal, A. Optics of photonic quasicrystals. *Nat. Photonics* **7**, 177–187 (2013).
 - [9] Kohmoto, M., Sutherland, B. & Iyuchi, K. Localization of optics: Quasiperiodic media. *Phys. Rev. Lett.* **58**, 2436–2438 (1987).
 - [10] Edagawa, K. Photonic crystals, amorphous materials, and quasicrystals. *Sci. Technol. Adv. Mater.* **15**, 034805 (2014).
 - [11] Rechtsman, M. C., Jeong, H.-C., Chaikin, P. M., Torquato, S. & Steinhardt, P. J. Optimized structures for photonic quasicrystals. *Phys. Rev. Lett.* **101**, 073902 (2008).
 - [12] Peach, M. Quasicrystals step out of the shadows. *Mater. Today* **9**, 44–47 (2006).
 - [13] Kraus, Y. E., Lahini, Y., Ringel, Z., Verbin, M. & Zilberberg, O. Topological states and adiabatic pumping in quasicrystals. *Phys. Rev. Lett.* **109**, 106402 (2012).
 - [14] Verbin, M., Zilberberg, O., Kraus, Y. E., Lahini, Y. & Silberberg, Y. Observation of topological phase transitions in photonic quasicrystals. *Phys. Rev. Lett.* **110**, 076403 (2013).
 - [15] Verbin, M., Zilberberg, O., Lahini, Y., Kraus, Y. E. & Silberberg, Y. Topological pumping over a photonic Fibonacci quasicrystal. *Phys. Rev. B* **91**, 064201 (2015).
 - [16] Kollár, A., Fitzpatrick, M. & Houck, A. Hyperbolic lattices in circuit quantum electrodynamics. *Nature* **571**, 45–50 (2019).
 - [17] Yang, Z., Lustig, E., Lumer, Y. & Segev, M. Photonic Floquet topological insulators in a fractal lattice. *Light Sci. Appl.* **9**, 32704361 (2020).
 - [18] Carr, S. *et al.* Twistronics: Manipulating the electronic properties of two-dimensional layered structures through their twist angle. *Phys. Rev. B* **95**, 075420 (2017).

- 352 [19] Bellissard, J. & Simon, B. Cantor spectrum for the almost Mathieu equation. *J. Funct. Anal.* **48**, 408–419 (1982).
- 353 [20] Etter, S., Massatt, D., Luskin, M. & Ortner, C. Modeling and computation of Kubo conductivity for two-dimensional
354 incommensurate bilayers. *Multiscale Model. Simul.* **18**, 1525–1564 (2020).
- 355 [21] Rosa, M. I. N., Ruzzene, M. & Prodan, E. Topological gaps by twisting. *Commun. Phys.* **4**, 130 (2021).
- 356 [22] Bergman, D. J. Exactly solvable microscopic geometries and rigorous bounds for the complex dielectric constant of a
357 two-component composite material. *Phys. Rev. Lett.* **44**, 1285–1287 (1980).
- 358 [23] Milton, G. W. Bounds on the complex dielectric constant of a composite material. *Appl. Phys. Lett.* **37**, 300–302 (1980).
- 359 [24] Golden, K. & Papanicolaou, G. Bounds for effective parameters of heterogeneous media by analytic continuation. *Comm.*
360 *Math. Phys.* **90**, 473–491 (1983).
- 361 [25] Milton, G. W. *The Theory of Composites*. Cambridge Monographs on Applied and Computational Mathematics (Cam-
362 bridge University Press, 2002).
- 363 [26] Murphy, N. B., Cherkaev, E., Hohenegger, C. & Golden, K. M. Spectral measure computations for composite materials.
364 *Commun. Math. Sci.* **13**, 825–862 (2015).
- 365 [27] Murphy, N. B., Cherkaev, E. & Golden, K. M. Anderson transition for classical transport in composite materials. *Phys.*
366 *Rev. Lett.* **118**, 036401 (2017).
- 367 [28] Golden, K., Goldstein, S. & Lebowitz, J. L. Classical transport in modulated structures. *Phys. Rev. Lett.* **55**, 2629–2632
368 (1985).
- 369 [29] Golden, K., Goldstein, S. & Lebowitz, J. L. Discontinuous behavior of effective transport coefficients in quasiperiodic
370 media. *J. Stat. Phys.* **58**, 669–684 (1990).
- 371 [30] Simon, B. Almost periodic Schrödinger operators: A review. *Adv. Appl. Math.* **3**, 463–490 (1982).
- 372 [31] Ostlund, S., Prandit, R., Rand, D., Schnellhuber, H. J. & Siggia, E. D. One dimensional Schrödinger equation with an
373 almost periodic potential. *Phys. Rev. Lett.* **50**, 1873–1877 (1983).
- 374 [32] Kohmoto, M. & Oono, Y. Cantor spectrum for an almost periodic Schrödinger equation and a dynamical map. *Phys. Lett.*
375 *A* **102**, 145–148 (1984).
- 376 [33] Arakelian, S. *et al.* Formation of quasiperiodic bimetal thin films with controlled optical and electrical properties. In
377 Andrews, D. L., Nunzi, J.-M. & Ostendorf, A. (eds.) *Nanophotonics VI*, vol. 9884, 509 – 516. International Society for
378 Optics and Photonics (SPIE, 2016).
- 379 [34] Nandhagopal, P., Pal, A. K. & Bharathi Mohan, D. Fabrication of silver and silver-copper bimetal thin films using
380 co-sputtering for SERS applications. *Opt. Mater.* **97**, 109381 (2019).
- 381 [35] Genov, D. A., Sarychev, A. K., Shalaev, V. M. & Wei, A. Resonant field enhancements from metal nanoparticle arrays.
382 *Nano Lett.* **4**, 153 – 158 (2004).
- 383 [36] Genov, D. A., Shalaev, V. M. & Sarychev, A. K. Surface plasmon excitation and correlation-induced localization-
384 delocalization transition in semicontinuous metal films. *Phys. Rev. B* **72**, 113102 (2005).
- 385 [37] Dallapiccola, R., Gopinath, A., Stellacci, F. & Negro, L. D. Quasi-periodic distribution of plasmon modes in two-
386 dimensional Fibonacci arrays of metal nanoparticles. *Opt. Express* **16**, 5544–5555 (2008).
- 387 [38] Shenhar, R. & Rotello, V. Nanoparticles: Scaffolds and building blocks. *Acc. Chem. Res.* **36**, 549–561 (2003).
- 388 [39] Bergman, D. J. & Stroud, D. Physical properties of macroscopically inhomogeneous media. *Phys. Solid State* **46**, 147–269
389 (1992).
- 390 [40] Clerc, J. P., Giraud, G., Laugier, J. M. & Luck, J. M. The electrical conductivity of binary disordered systems, percolation
391 clusters, fractals, and related models. *Adv. Phys.* **39**, 191–309 (1990).
- 392 [41] Jonckheere, T. & Luck, J. M. Dielectric resonances of binary random networks. *J. Phys. A Math. Theor.* **31**, 3687–3717
393 (1998).
- 394 [42] Stauffer, D. & Aharony, A. *Introduction to Percolation Theory, Second Edition* (Taylor and Francis, London, 1992).
- 395 [43] Torquato, S. *Random Heterogeneous Materials: Microstructure and Macroscopic Properties* (Springer-Verlag, New York,
396 2002).
- 397 [44] Cherkaev, E. Inverse homogenization for evaluation of effective properties of a mixture. *Inverse Probl.* **17**, 1203–1218
398 (2001).
- 399 [45] Losurdo, M., Moreno, F., Cobet, C., Modreanu, M. & Pernice, W. Plasmonics: Enabling functionalities with novel
400 materials. *J. Appl. Phys.* **129**, 220401 (2021).
- 401 [46] Zhang, S. *et al.* Abnormal conductivity in low-angle twisted bilayer graphene. *Sci. Adv.* **6**, eabc5555 (2020).
- 402 [47] Guhr, T., Müller-Groeling, A. & Weidenmüller, H. A. Random-matrix theories in quantum physics: Common concepts.
403 *Phys. Rep.* **299**, 189–425 (1998).
- 404 [48] Canali, C. M. Model for a random-matrix description of the energy-level statistics of disordered systems at the Anderson
405 transition. *Phys. Rev. B* **53**, 3713–3730 (1996).